The Extended [C II] under Construction? Observation of the Brightest High-z Lensed Star-forming Galaxy at z = 6.2

Yoshinobu Fudamoto[1,2,3], Akio K. Inoue[2,4], Dan Coe[5,6,7], Brian Welch[8,9,10], Ana Acebron[11,12], Massimo Ricotti[13], Nir Mandelker[14], Rogier A. Windhorst[15], Xinfeng Xu[16], Yuma Sugahara[2,3], Franz E. Bauer[17,18,19], Maruša Bradač[20,21], Larry D. Bradley[5], Jose M. Diego[22], Michael Florian[23], Brenda Frye[23], Seiji Fujimoto[24], Takuya Hashimoto[25,26], Alaina Henry[5,7], Guillaume Mahler[27,28], Pascal A. Oesch[29,30], Swara Ravindranath[5], Jane Rigby[9], Keren Sharon[31], Victoria Strait[32,33], Yoichi Tamura[34], Michele Trenti[35,36], Eros Vanzella[37], Erik Zackrisson[38], and Adi Zitrin[39]

[1] Center for Frontier Science, Chiba University, 1-33 Yayoi-cho, Inage-ku, Chiba 263-8522, Japan; yoshinobu.fudamoto@gmail.com
[2] Waseda Research Institute for Science and Engineering, Faculty of Science and Engineering, Waseda University, 3-4-1 Okubo, Shinjuku, Tokyo 169-8555, Japan
[3] National Astronomical Observatory of Japan, 2-21-1, Osawa, Mitaka, Tokyo, Japan
[4] Department of Physics, School of Advanced Science and Engineering, Faculty of Science and Engineering, Waseda University, 3-4-1, Okubo, Shinjuku, Tokyo 169-8555, Japan
[5] Space Telescope Science Institute (STScI), 3700 San Martin Drive, Baltimore, MD 21218, USA
[6] Association of Universities for Research in Astronomy (AURA) for the European Space Agency (ESA), STScI, Baltimore, MD, USA
[7] Center for Astrophysical Sciences, Department of Physics and Astronomy, The Johns Hopkins University, 3400 N Charles Street, Baltimore, MD 21218, USA
[8] Department of Astronomy, University of Maryland, College Park, MD 20742, USA
[9] Observational Cosmology Lab, NASA Goddard Space Flight Center, Greenbelt, MD 20771, USA
[10] Center for Research and Exploration in Space Science and Technology, NASA/GSFC, Greenbelt, MD 20771, USA
[11] Dipartimento di Fisica, Università degli Studi di Milano, Via Celoria 16, I-20133 Milano, Italy
[12] INAF—IASF Milano, via A. Corti 12, I-20133 Milano, Italy
[13] Department of Astronomy, University of Maryland, College Park, MD 20742, USA
[14] Centre for Astrophysics and Planetary Science, Racah Institute of Physics, The Hebrew University, Jerusalem, 91904, Israel
[15] School of Earth and Space Exploration, Arizona State University, Tempe, AZ 85287-1404, USA
[16] Center for Astrophysical Sciences, Department of Physics and Astronomy, Johns Hopkins University, Baltimore, MD 21218, USA
[17] Instituto de Astrofísica, Facultad de Física, Pontificia Universidad Católica de Chile, Campus San Joaquín, Av. Vicuña Mackenna 4860, Macul Santiago, 7820436, Chile
[18] Centro de Astroingeniería, Facultad de Física, Pontificia Universidad Católica de Chile, Campus San Joaquín, Av. Vicuña Mackenna 4860, Macul Santiago, 7820436, Chile
[19] Millennium Institute of Astrophysics, Nuncio Monseñor Sótero Sanz 100, Of 104, Providencia, Santiago, Chile
[20] University of Ljubljana, Department of Mathematics and Physics, Jadranska ulica 19, SI-1000 Ljubljana, Slovenia
[21] Department of Physics and Astronomy, University of California Davis, 1 Shields Avenue, Davis, CA 95616, USA
[22] Instituto de Física de Cantabria (CSIC-UC). Avda. Los Castros s/n. E-39005 Santander, Spain
[23] Department of Astronomy, Steward Observatory, University of Arizona, 933 North Cherry Avenue, Tucson, AZ 85721, USA
[24] Department of Astronomy, The University of Texas at Austin, Austin, TX 78712, USA
[25] Division of Physics, Faculty of Pure and Applied Sciences, University of Tsukuba, Tsukuba, Ibaraki 305-8571, Japan
[26] Tomonaga Center for the History of the Universe (TCHoU), Faculty of Pure and Applied Sciences, University of Tsukuba, Tsukuba, Ibaraki 305-8571, Japan
[27] Institute for Computational Cosmology, Durham University, South Road, Durham DH1 3LE, UK
[28] Centre for Extragalactic Astronomy, Durham University, South Road, Durham DH1 3LE, UK
[29] Departement d'Astronomie, Université de Genéve, 51 Ch. Pegasi, CH-1290 Versoix, Switzerland
[30] Cosmic Dawn Center (DAWN), Niels Bohr Institute, University of Copenhagen, Jagtvej 128, København N, DK-2200, Denmark
[31] Department of Astronomy, University of Michigan, 1085 S. University Avenue, Ann Arbor, MI 48109, USA
[32] Cosmic Dawn Center (DAWN), Copenhagen, Denmark
[33] Niels Bohr Institute, University of Copenhagen, Jagtvej 128, Copenhagen, Denmark
[34] Department of Physics, Graduate School of Science, Nagoya University, Aichi 464-8602, Japan
[35] School of Physics, University of Melbourne, Parkville 3010, VIC, Australia
[36] ARC Centre of Excellence for All Sky Astrophysics in 3 Dimensions (ASTRO 3D), Australia
[37] INAF—OAS, Osservatorio di Astrofisica e Scienza dello Spazio di Bologna, via Gobetti 93/3, I-40129 Bologna, Italy
[38] Observational Astrophysics, Department of Physics and Astronomy, Uppsala University, Box 516, SE-751 20 Uppsala, Sweden
[39] Physics Department, Ben-Gurion University of the Negev, P.O. Box 653, Be'er-Sheva 84105, Israel

Abstract

We present results of [C II] 158 μm emission line observations, and report the spectroscopic redshift confirmation of a strongly lensed ($\mu \sim 20$) star-forming galaxy, MACS0308-zD1 at $z = 6.2078 \pm 0.0002$. The [C II] emission line is detected with a signal-to-noise ratio >6 within the rest-frame UV-bright clump of the lensed galaxy (zD1.1) and exhibits multiple velocity components; the narrow [C II] has a velocity full width half maximum (FWHM) of 110 ± 20 km s^{-1}, while broader [C II] is seen with an FWHM of 230 ± 50 km s^{-1}. The broader [C II] component is blueshifted (-80 ± 20 km s^{-1}) with respect to the narrow [C II] component, and has a morphology that extends beyond the UV-bright clump. We find that, while the narrow [C II] emission is most likely associated with zD1.1, the broader component is possibly associated with a physically distinct gas component from zD1.1 (e.g.,

outflowing or inflowing gas). Based on the nondetection of $\lambda_{158\,\mu m}$ dust continuum, we find that MACS0308-zD1's star formation activity occurs in a dust-free environment indicated by a strong upper limit of infrared luminosity $\lesssim 9 \times 10^8 \, L_\odot$. Targeting this strongly lensed faint galaxy for follow-up Atacama Large Millimeter/submillimeter Array and JWST observations will be crucial to characterize the details of typical galaxy growth in the early Universe.

Unified Astronomy Thesaurus concepts: High-redshift galaxies (734); Galaxy evolution (594); Galaxy formation (595); Gravitational lensing (670)

1. Introduction

Over the past decades, optical/near-infrared surveys using ground- and space-based telescopes have built large samples of high-redshift galaxies at $z > 6$, revealing star formation activity and stellar mass buildup in the first Gyr of the Universe (e.g., Madau & Dickinson 2014; Stefanon et al. 2021; Weaver et al. 2023). Recently, our understanding of early galaxy buildup has been significantly advanced by unprecedented sensitivity and high-resolution observations of the Atacama Large Millimeter/submillimeter Array (ALMA). ALMA observations have built large samples of of high-redshift galaxies with strong far-infrared emission lines (e.g., [C II] 158 μm, [O III] 88 μm) and dust continuum (e.g., Hashimoto et al. 2018; Béthermin et al. 2020; Fudamoto et al. 2021; Bouwens et al. 2022), and ultimately revealing the interstellar medium (ISM) properties of these early epoch galaxies.

ALMA [C II] 158 μm emission line surveys have so far revealed ISM properties for > 100 for galaxies at high redshift, including the following: galaxy-scale morpho-kinematics, which suggest a large diversity of formation pathways among $z > 4$ star-forming galaxies (Le Fèvre et al. 2020; Jones et al. 2021); ~ 500–1000 km s^{-1} gas outflows velocities (Maiolino et al. 2012; Ginolfi et al. 2020); and ~ 30 kpc scale gas halos surrounding a dominant fraction of galaxies, which imply a star formation driven metal pollution of the circumgalactic medium (Fujimoto et al. 2020; Fudamoto et al. 2022). A strong correlation between the neutral gas reservoir can be seen in [C II] and star formation rate (SFR) of galaxies (Schaerer et al. 2020). Evolution of dust-obscured star formation activities suggests an evolution of dust attenuation properties at $z > 4$ (Bouwens et al. 2020; Fudamoto et al. 2020). It has been proposed to use [C II] 158 μm line as a tracer of star-forming neutral gas, which shows evolution of the neutral gas fraction of high-redshift galaxies (Zanella et al. 2018; Dessauges-Zavadsky et al. 2020; Heintz et al. 2021).

To date, these high-z observations have been mostly limited to massive star-forming galaxies (i.e., $M_* > 10^{10} \, M_\odot$ and/or SFR $> 10 \, M_\odot$ yr^{-1}), and we only have small samples of less evolved, low-mass/low-SFR galaxies. This is because detailed ISM observations of relatively low-mass galaxies are still one of the major challenges even for ALMA as they are intrinsically faint. One method to push to fainter limits is to adopt strongly lensed galaxies to investigate the detailed properties of high-redshift, low-mass galaxies in a feasible observing time (e.g., Coe et al. 2019; Treu et al. 2022; Vanzella et al. 2023).

Once such strongly magnified high-redshift sources are identified and their redshifts are confirmed, they become prioritized for several follow-up observations to study gas kinematics, ionized/neutral gas conditions, and their spatial distributions; e.g., A1689-zD1 (Watson et al. 2015; Akins et al. 2022), A383-5.1 (Knudsen et al. 2016), RXJ1347:1216 (Bradač et al. 2017), MACS0416_Y1 (Tamura et al. 2019;

Bakx et al. 2020), MACS1149-JD1 (Hashimoto et al. 2018; Carniani et al. 2020), A1703-zD1 (Schaerer et al. 2015; Molyneux et al. 2022), MACSJ0416-D1 (Vanzella et al. 2019; Calura et al. 2021), RXCJ0600-z6 (Fujimoto et al. 2021), and MACS0454-1251 (Glazer et al. 2023). The number of identified magnified low-mass sources are, however, still limited, and the study of the ISM properties of low-mass, high-z galaxies is thus still in its nascent stages.

Here, we report an observation of a strongly lensed $\sim L*$ star-forming galaxy: MACS0308-zD1 at $z \sim 6.2$. We clearly detect a [C II] 158 μm emission line and measure the spectroscopic redshift of MACS0308-zD1 for the first time (Acebron et al. 2018; Salmon et al. 2020; Welch et al. 2023). Making use of high-resolution, high-sensitivity ALMA observations, we also study the velocity structure and morphology of the [C II] emission. These suggest multiple components of [C II] emission that are distinct in spatial and spectral directions.

This paper is organized as follows: In Section 2, we describe our target galaxy and the ALMA observations used in this study. In Section 3, we present our data analysis and measurements for the [C II] 158 μm emission line and $\lambda_{\rm rest} \sim 158$ μm dust continuum. In Section 4, we compare to previous studies and discuss our results. Finally, we conclude with the summary in Section 5. Throughout this paper, we assume a cosmology with $(\Omega_m, \Omega_\Lambda, h) = (0.3, 0.7, 0.7)$, and the Chabrier (Chabrier 2003) initial mass function, where applicable. With these cosmological parameters, $1''$ corresponds to 5.6 kpc at $z = 6.2078$.

2. Observation and Data Reduction

2.1. Target: MACS0308-zD1

The target of the ALMA observations, MACS0308-zD1, was identified in the Reionization Lensing Cluster Survey (RELICS; Coe et al. 2019) in the background of the lensing cluster MACS0308+26. The galaxy was first identified as one of the triply imaged galaxies in the field at $z > 6$ (Acebron et al. 2018), and our target is the brightest among the three images (R. A. $= 03 : 08 : 53.407$, decl. $= + 26 : 44 : 58.93$, which originally given the ID of MACS0308-c4.3 in Acebron et al. 2018). MACS0308-zD1 was found as the apparently UV-brightest $z > 6$ galaxy having $m_{\rm AB} = 23.0$ mag, and an estimated photometric redshift of $z_{\rm ph} \sim 6.2$–6.3 (Salmon et al. 2020). Welch et al. (2023) further analyzed MACS0308-zD1 by forward modeling of the galaxy in the source plane and found an updated robust photometric redshift of $z_{\rm ph} = 6.21$, and that MACS0308-zD1 consists of a bright clump: MACS0308-zD1.1, and a faint diffuse component. The bright clump was found to have a radius of $r = 27 \pm 5$ pc in its source plane, and to have an extremely high-SFR surface density of $\Sigma_{\rm SFR} = 900 \pm 300 \, M_\odot$ yr^{-1} kpc^{-2}. This $\Sigma_{\rm SFR}$ is the highest value ever found at $z \sim 6$ star-forming galaxies (Kennicutt & Evans 2012), suggesting that the clump
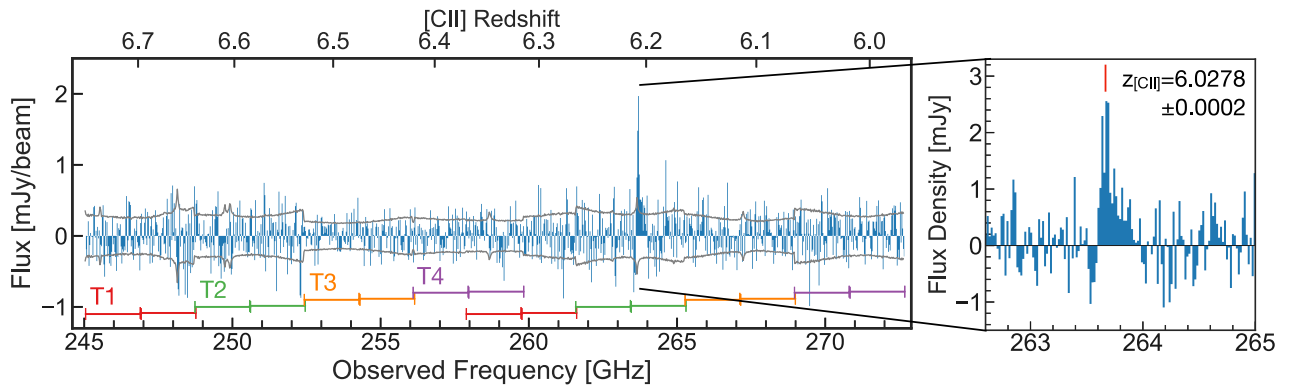
Figure 1. Left panel: the entire spectrum of the MACS0308-zD1 using a spectral bin width of 30 km s^{-1}. The spectrum is extracted from a peak pixel of the line moment-0 map. Dust continuum was not subtracted as it is not detected. The gray line shows the pixel-by-pixel RMS of each channel. An emission line is significantly detected at the frequency of 263.700 ± 0.004 GHz confirming a spectroscopic redshift of $z_{[CII]}$ = 6.2078 ± 0.0002. The bottom horizontal solid lines indicate the frequency coverage of each tuning (T1 to T4). Right panel: zoomed-in view of the spatially integrated [C II] emission line of MACS0308-zD1 with a spectral bin width of 20 km s^{-1}. The integrated spectrum was extracted using the 2σ area within its moment-0 map. The [C II] line has a skewed profile that suggests the existence of multiple velocity components in the [C II] emission (see Section 3.2).

could be an environment similar to the starburst galaxies. The diffuse component of MACS0318-zD1 has a radius of $r = 900 \pm 200$ pc, and has $\Sigma_{SFR} \sim 0.22 \pm 0.08 \, M_\odot \, \mathrm{yr}^{-1} \, \mathrm{kpc}^{-2}$. Detailed source plane analysis in Welch et al. (2023), thus, showed that MACS0318-zD1 consists of higly star-forming clump and a diffuse extended structure.

MACS0308-zD1 is found to be gravitationally magnified by a factor of ∼20 (Acebron et al. 2018; Salmon et al. 2020; Welch et al. 2023). However, such a large magnification factor is usually uncertain. Zitrin et al. (2015) found a typical uncertainty of ∼60% for a magnification factor of ∼20 depending lens models. Further, magnification changes across the stretched structure of the galaxy. While the bright clump has a magnification of 22, the farthest tail has a magnification of 15 (Welch et al. 2023). In this paper, we use a fiducial magnification factor of $\mu = 20$ for our analysis, and apply a conservative systemic uncertainty of 60% for the magnification factor where applicable.

2.2. ALMA Observations

MACS0308-zD1 has been observed in the ALMA program #2021.1.00143.S (PI: Fudamoto). The observation scanned to search the [C II] 158 μm emission line at a sky frequency range between 245 and 273 GHz that covers entire photometric redshift probability of the target (Acebron et al. 2018; Salmon et al. 2020; Welch et al. 2023). To efficiently scan the frequency range, the observations used four separate spectral tunings (T1 to T4; see Figure 1). The correlator was set up in dual polarization and frequency domain mode, covering 1.875 GHz bandwidth having a native spectral resolution of ∼9 km s^{-1}.

All tunings were observed during multiple observing runs using the ALMA cycle-8 C43-3 configuration. The on-source time was ∼0.5, ∼1.6, ∼1.0, and ∼1.0 hr, respectively. The precipitable water vapor (PWV) during the observations was 0.545, 1.450, 0.544, 0.636 mm for tunings T1, T2, T3, and T4, respectively. The relatively large variations of the on-source time were mainly due to variations in the weather conditions.

For the data calibration, we asked East Asian ALMA Regional Center for the data calibration support[40] to deliver the

calibrated data that are produced using the pipeline code created during the second quality assurance procedure (i.e., `ScriptForPI.py`). The observed data were analyzed using The Common Astronomy Software Application (CASA) version 6.2.1 (CASA Team et al. 2022).

2.3. Imaging Data Cube and [C II] 158 μm Line Detection

To search the [C II] 158 μm emission line, we created a data cube combining all four tunings using CASA task `tclean` using `NATURAL` weighting scheme, a spectral binning of 30 km s^{-1}, a pixel scale of 0."1, and an image size of 30″ × 30″ (i.e., a large enough sky area that contains the primary beam attenuation <50%). With CASA task `tclean`, we performed the synthesized beam deconvolution using a fixed stopping threshold of 3 times the pixel-by-pixel RMS for all channels and the maximum iteration of 500 times. The RMSs were separately calculated and used for `tclean` processes of each T1, T2, T3, and T4 tuning data to take into account the variations of the average RMS of each tunings. The conservative deconvolution threshold does not affect the final data products as there are no bright sources in this velocity binning that could contaminate the resulting image products. The produced data cube has a synthesized beam full width at half maximum (FWHM) of 1."31 × 0."73, 0."94 × 0."68, 1."11 × 0."78, and 1."03 × 0."73 for tunings 1, 2, 3, and 4, respectively. The achieved average pixel-by-pixel RMSs are 0.28, 0.30, 0.21, 0.23 mJy beam^{-1} with 30 km s^{-1} bins, for T1, T2, T3, and T4, respectively. The variations in the sensitivity by a factor of up to 1.4 are due to the variations of the PWV under which each tuning was observed and also due to the weak atmospheric absorption features (see Figure 1).

Using the location of the rest-frame UV emission as a prior of the spatial position of [C II], we found the [C II] 158 μm emission line from MACS0308-zD1 at a frequency of 263.6995 ± 0.004 GHz (Figure 1).

2.4. Imaging Continuum Map

The $\lambda_{rest} \sim 158 \, \mu$m continuum image of MACS0308-zD1 was created using CASA task `tclean` with the multifrequency synthesis mode. During the continuum imaging, we conservatively excluded the whole spectral window that contains the entire [C II] 158 μm emission line. Since we only

---

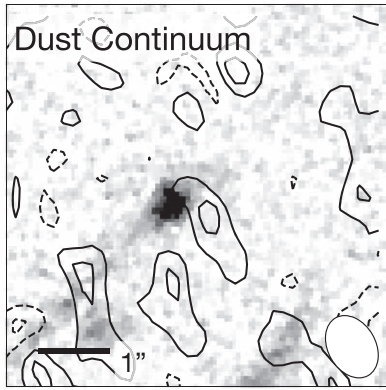**Figure 2.** $6'' \times 6''$ cutout of HST F160W image (background) and dust continuum (contours). Solid (dashed) contours show 1σ, 2σ (-2σ, -1σ) signals of the dust continuum image. The astrometry of HST F160W is matched to the GAIA 3rd data release (DR3) coordinates (Gaia Collaboration et al. 2023). The white ellipse in the lower right corner shows the synthesized beam FWHM of the continuum image. As there is no significant signal spatially colocated with the rest-frame UV detections in the HST image, we conclude that the dust continuum of MACS0308-zD1 is nondetected in our observations, and we provided a flux 3σ upper limit of $<27\,\mu$Jy.

excluded one spectral window out of the 16 total spectral windows from our four spectral setups, the exclusion does not affect the resulting sensitivity of the continuum map. The synthesized beam deconvolution was performed using NAT-URAL weighting scheme, using a stopping threshold of $27\,\mu$Jy beam^{-1} (i.e., $3 \times$ the pixel-by-pixel RMS of the dirty image) and by setting the maximum number of iteration to 500 times. Again, the deconvolution thresholds do not affect the result, as there are no bright sources in the continuum image. As a result, we obtained a dust continuum image of MACS0308-zD1 that has a final pixel-by-pixel RMS of $8.9\,\mu$Jy beam^{-1} (Figure 2).

3. Analysis and Measurements

3.1. Dust Continuum

In the continuum image, there is only a $\sim 2\sigma$ positive signal close to but offset from the rest-frame UV position of the MACS0308-zD1 (Figure 2). Several previous studies found that typically a significance of $>3.5\sigma$ is required to avoid contamination of noise signals (e.g., Béthermin et al. 2020; Inami et al. 2022). Therefore, we conclude that the dust continuum of MACS0308-zD1 is not detected neither from the bright clump MACS0308-zD1.1 or diffuse component.

As the dust continuum is not detected, we estimated the 3σ upper limit of the rest-frame $158\,\mu$m continuum of whole MACS0308-zD1 as $<27\,\mu$Jy, adopting $3 \times$ the pixel-by-pixel RMS. Assuming a dust temperature of ~ 45 K and $\beta = 1.8$ (Béthermin et al. 2020; Sommovigo et al. 2022) for a modified blackbody emission, we estimated a 3σ upper limit of the observed infrared (IR) luminosity of $<1.9 \times 10^{10}\,L_\odot$ in the image plane. This means $L_{\rm IR} < 9.5 \times 10^{8}\,L_\odot$ in the source plane assuming $\mu = 20$.

3.2. [C II] 158 μm Emission Line

We extracted the [C II] emission line and created the moment-0 map in an iterative way. First, we created a moment-0 map integrating over an arbitrary frequency range that clearly include the [C II] emission line. Second, we
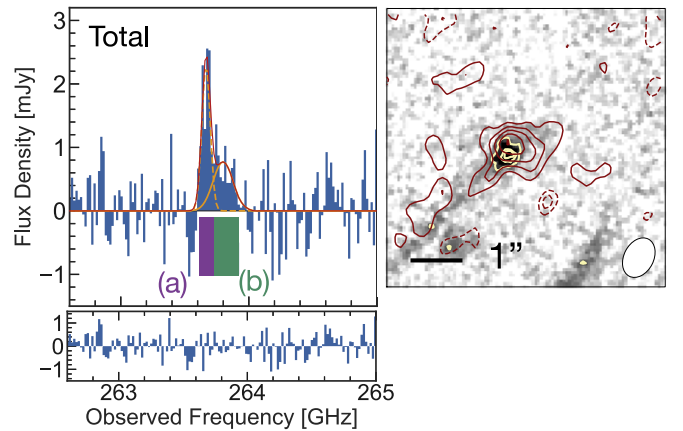

Figure 3. Left panel: the [C II] 158 μm emission line integrated over entire components. The red line shows the result of two-component 1D Gaussian fitting to the spectra. Orange lines show individual Gaussians for narrow (dashed line) and broader (solid line) components. The residuals of the fits are indicated in the lower inset. The inset shows that there are no noticeable residuals by comparing to the rest of the frequency range. The frequency ranges indicated with the boxes (a) and (b) are used to make individual moment-0 images for the narrow and the broader components (Section 3.3; see also Figure 4). Right panel: $6'' \times 6''$ cutout of HST F160W image with [C II] moment-0 contours (red solid contours, 2σ–6σ; red dashed contours, -3σ, -2σ). Yellow contours show 5σ, 15σ, 25σ of the F160W image. The moment-0 map is made by integrating 263.6–263.99 GHz. The white ellipse in the lower right corner shows the synthesized beam FWHM of the moment-0 image. Astrometry of the HST image is matched to the GAIA DR3 catalog (Gaia Collaboration et al. 2023).

extracted the [C II] spectrum using the moment-0 maps as a mask. Namely, we used pixels that had $>2\sigma$ signals in the moment-0 map, and extracted integrated spectra that were again used to create moment-0 map using the channels having continuous positive signals. The procedures are repeated until the channels used to create moment-0 map converged. A few iterations were enough to converge, with the final results shown in Figure 3.

In this way, we obtained the moment-0 image and the spectrum of the [C II] emission line integrated over the whole galaxy component. As a result, we found that [C II] emission line of MACS0308-zD1 is detected from the bright clump MACS0308-zD1.1. We did not find any clear [C II] emission line from the diffuse component. Using the integrated moment-0 map, we measured the total [C II] flux density using CASA task imfit; 2D Gaussian fitting. The measured quantities are summarized in Table 1.

3.3. Multicomponent Analysis of the [C II] line

The [C II] emission line of MACS0308-zD1.1 deviates from a single Gaussian profile, and shows a blueshifted excess (Figure 3). We separated these components and estimated the properties of each of the [C II] lines. As a first step, we performed a least square fitting using a two-component Gaussian function to the integrated 1D spectrum of the [C II] emission. This resulted in a reasonable fit with only small residuals that were consistent with random noise. We found that the best fitting results arose from the combination of a narrow and a broader Gaussian (left panel of Figure 3).

We then created moment-0 maps for both the narrow and the broader [C II] emission by integrating frequency ranges of 263.62–263.72 GHz and 263.73–263.92 GHz, respectively. These frequency ranges were selected to separately image

Table 1
Summary of the ALMA Measurements

[C II] Component	Redshift	[C II] FWHM (km s^{-1})	$f_{[CII]} \times \mu^a$ (Jy km s^{-1})	$L_{[CII]}$ ($L_\odot$)	M_{H_2} ($M_\odot$)
Total	6.2078 ± 0.0002	...	0.62 ± 0.18	$3.0 \pm 1.9 \times 10^7$	$9.1 \pm 5.5 \times 10^8$
Narrow	6.2078 ± 0.0002	110 ± 20	0.37 ± 0.10	$1.7 \pm 1.1 \times 10^7$	$5.1 \pm 3.1 \times 10^8$
Broad	6.2058 ± 0.0005	230 ± 50	0.30 ± 0.09	$1.4 \pm 0.9 \times 10^7$	$4.1 \pm 2.5 \times 10^8$

Note. We used the single-component 2D Gaussian fits to measure integrated fluxes.
[a] The measured values (except for the [C II] flux densities) are corrected for gravitational lensing magnification of $\mu = 20$ with 60% of systematic uncertainties quadratically added.

moment-0 maps of the two different components, and at the same time, to avoid contamination of different components.

Based on the results of the two-component Gaussian fitting, we estimated the fractions of contamination for each maps. Using the above frequency range to integrate and the results of the two-component Gaussian fitting, we estimated that ∼7% of the narrow [C II] component contaminates the broad image, while ∼8% of the broader [C II] component contaminates the narrow [C II] moment-0 maps. Thus, the contamination from other components has only a minor impact on the moment-0 maps and measured fluxes for each component.

3.3.1. The Narrow [C II] Emission Component

The moment-0 image of the narrow [C II] component shows a 6σ detection. The emission is cospatial with the rest-frame UV emission of the bright clump: MACS0308-zD1.1 seen by the HST F160W filter (top panel of Figure 4). The significant detection from the cospatial location implies that the narrow component is associated with the UV-bright star formation activity of the MACS0308-zD1.1 and not associated with the underlying diffuse component. We extracted the narrow component of the [C II] emission using the moment-0 map (top left panel of Figure 4). We measured a velocity FWHM of the narrow component by fitting 1D Gaussian and found the FWHM of 110 ± 20 km s^{-1}. We note that the line width lies at the lower bound of the FWHM of [C II] emission lines thus far observed from high-redshift galaxies (e.g., Béthermin et al. 2020).

3.3.2. The Broader [C II] Emission Component

The moment-0 image of the broader [C II] shows a $\sim 4.2\sigma$ detection. The emission appears somewhat offset from rest-frame UV emission of the MACS0308-zD1.1 (bottom panel of Figure 4). We measured a velocity FWHM of the broader [C II] component using the same 1D Gaussian fitting proceder and found the velocity FWHM of 230 ± 50 km s^{-1}, roughly 2 times broader than the narrow component. The broader component appears blueshifted by $\Delta v = -80 \pm 20$ km s^{-1} with respect to the narrow component (Table 1).

4. Discussion

4.1. Dust-obscured Star Formation Activity

We derive a 3σ upper limit to the observed IR luminosity of $< 1.9 \times 10^{10} L_\odot$ assuming a dust temperature of 45 K. The 3σ upper limit IR luminosity in the source plane is $\lesssim 9 \times 10^8 L_\odot$, applying a magnification factor of $\mu = 20$. The strong upper limit on the IR luminosity implies an extremely low dust-obscured SFR of SFR$_{IR} < 0.1 M_\odot$ yr^{-1} using the conversion of
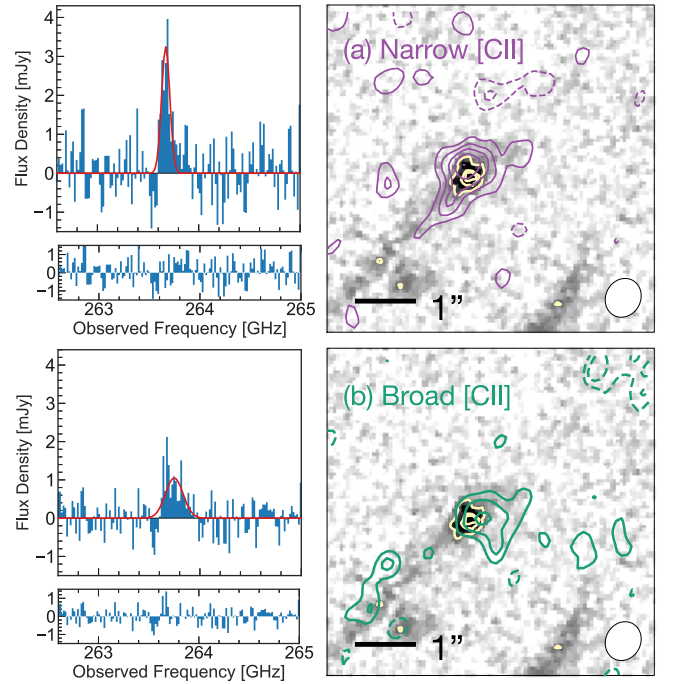

Figure 4. Left panels: the extracted [C II] 158 μm spectrum using pixels with $> 2\sigma$ significance in the moment-0 maps. The red lines show the results of single-component 1D Gaussian fitting to the spectra. The residuals of the fits are indicated in the lower insets. Right panels show $6'' \times 6''$ cutouts of HST F160W image (astrometry corrected using GAIA DR3; Gaia Collaboration et al. 2023) with [C II] moment-0 contours (purple or green solid contours, 2σ–6σ; purple or green dashed contours, -3σ, -2σ). Yellow contours show 5σ, 15σ, 25σ of the F160W image. The white ellipse in the lower right corner shows the synthesized beam FWHM of the moment-0 image. Top: [C II] emission line integrated over the narrow component. The moment-0 map is made by integrating 263.62–263.72 GHz. Bottom: broader component of [C II] emission. The moment-0 map is made by integrating 263.73–263.92 GHz. While the narrow [C II] is spatially colocated with the HST F160W detection, the broader [C II] appears somewhat offset from the rest–UV emission.

SFR$_{IR} = 1.2 \times 10^{-10} L_{IR} M_\odot$ yr$^{-1} L_\odot^{-1}$ (Madau & Dickinson 2014; Inami et al. 2022). Given the extreme brightness of MACS0308-zD1 in the rest-frame UV (SFR$_{UV} = 3 \pm 1 M_\odot$ yr^{-1} for zD1.1 and $7 \pm 2 M_\odot$ yr^{-1} for diffuse component; Welch et al. 2023), we derive a very low dust-obscured fraction of the star formation activity ($f_{obs} = $ SFR$_{IR}$/SFR$_{total}$) of only $\lesssim$1% to 3%, meaning that the star formation activity of MACS0308-zD1 is almost completely dust-free.

The major uncertainty in estimating the IR luminosity from a single ALMA observation is the unknown dust temperature; increasing the assumed dust temperature can produce larger IR luminosities (e.g., Faisst et al. 2020; Bakx et al. 2021; Fudamoto et al. 2023; Algera et al. 2023). We examined this

effect and its impact on the dust-obscured SFR. For a high dust temperature case of 60 K, the demagnified 3σ upper limit IR luminosity is $5.5 \times 10^9 L_\odot$, which yields a 3σ upper limit SFR of $\mathrm{SFR_{IR}} < 0.3 M_\odot \mathrm{yr}^{-1}$. Even for an extreme dust temperature of 80 K, we find $8.0 \times 10^9 L_\odot$ and $0.8 M_\odot \mathrm{yr}^{-1}$ for demagnified 3σ upper limit of IR luminosity and dust-obscured SFR, respectively. Although such extremely high dust temperatures are not yet confirmed in this redshift range (e.g., Algera et al. 2023), even with these extreme assumptions, we still derived low obscured fractions of star formation activity of $\lesssim 10\%$ ($T_\mathrm{d} = 60$ K) to $<26\%$ ($T_\mathrm{d} = 80$ K). Thus, MACS0308-zD1 has relatively little dust-obscured activity, even after accounting for rather extreme uncertainties in the dust temperature.

This low f_obs contrasts strongly with the relatively high obscured fractions ($\sim 50\%$) seen for massive $M_* > 10^{9.5} M_\odot$ galaxies at $z \gtrsim 5$ (Fudamoto et al. 2020; Schouws et al. 2022; Algera et al. 2023). Nonetheless, it is consistent with the very blue UV color of MACS0308-zD1 (UV slope of $\beta \sim -2.2$; Welch et al. 2023). The nearly dust-free environment is indicative of the metal-poor and young environment of the star formation activity. Recent studies found large [O III]/[C II] luminosity ratios from observations of such metal-poor and UV-bright galaxies (i.e., $L_\mathrm{[OIII]}/L_\mathrm{[CII]} \gtrsim 3$; Inoue et al. 2014; Hashimoto et al. 2019; Carniani et al. 2020). These studies argue that such high large [O III]/[C II] luminosity ratios of high-redshift galaxies might indicate low photodissociation region covering fractions, hard ionizing fields, and/or low metallicities (e.g., Harikane et al. 2020; Sugahara et al. 2022; Witstok et al. 2022). [O III] 88 μm emission line observations would be able to reveal such a high [O III]/[C II] can also be seen in the extremely star-forming condition of MACS0308-zD1.1. With the extremely high Σ_SFR, observations of MACS0308-zD1.1 may provide a sample to extend studies of star-forming conditions in high-redshift galaxies. Follow-up observations with ALMA will be important to further characterize conditions of the ISM of the star-forming region of the MACS0308-zD1.

4.2. [C II] 158 μm Emission Line

4.2.1. SFR–[C II] Correlation

It is highly debated whether the correlation between SFRs and $L_\mathrm{[CII]}$ evolves as a function of redshift. Previous studies have shown that galaxies with low SFRs or metallicities show extremely faint [C II] emission, denoted "[C II]-deficit" (e.g., Matthee et al. 2019; Harikane et al. 2020), that are also predicted by theoretical studies (e.g., Vallini et al. 2015; Liang et al. 2023). However, Schaerer et al. (2020) demonstrated that, based on large samples of galaxies obtained in the ALMA large program ALPINE (Béthermin et al. 2020; Faisst et al. 2020; Le Fèvre et al. 2020), there is no significant change of the observed $L_\mathrm{[CII]}$–SFR relation as a function of redshift, and pointed out that the previously obtained "[C II]-deficit" is largely affected by the uncertain estimations of the dust-obscured SFRs of high-redshift galaxies.

With the measured [C II] luminosity of MACS0308-zD1.1 and estimated SFR ($3 \pm 1 M_\odot \mathrm{yr}^{-1}$), MACS0308-zD1.1 appears consistent with the SFR–$L_\mathrm{[CII]}$ relation derived in the local galaxies (e.g., De Looze et al. 2014) and for high-redshift galaxies where no-evolution of the relation is found (Schaerer et al. 2020), but deviates from the "[C II]-deficit" relation suggested in some of the previous studies (Harikane et al. 2020; Liang et al. 2023). This is also true for the total galaxy
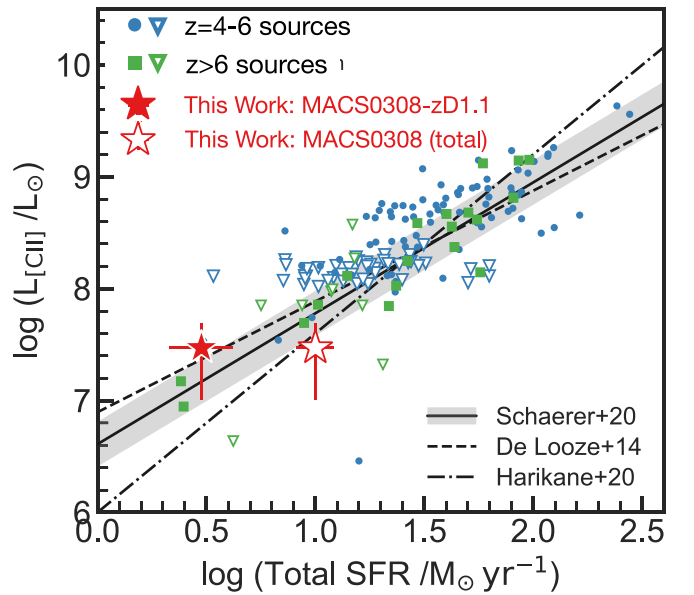

Figure 5. Observed [C II] luminosities vs. star formation rates of galaxies at $4 < z < 6$ (blue points and triangles; Schaerer et al. 2020 and references therein) and $z > 6$ (green squares and triangles; Matthee et al. 2019; Harikane et al. 2020; Glazer et al. 2023; Killi et al. 2023 and references therein). Downward triangles show 3σ upper limits of the [C II] nondetections. SFRs are estimated using SED fitting or dust attenuation corrections (i.e., the infrared excess–β relation; Fudamoto et al. 2020). Lines show previously derived relations for low- and high-redshift galaxies (solid, Schaerer et al. 2020; dashed, De Looze et al. 2014; and dotted–dashed, Harikane et al. 2020). The [C II] luminosity of MACS0308-zD1 remains consistent with the locally calibrated relation and the relation observed for $z \sim 5$ galaxies (De Looze et al. 2014; Schaerer et al. 2020), but lies well above from the relation with "[CII]-deficit" galaxies (Harikane et al. 2020).

MACS0308-zD1 (i.e., the bright clump plus the diffuse component; indicated by the white star in Figure 5). Here, we assume that the $\mathrm{SFR_{IR}}$ is negligible, given the faint IR luminosity upper limits and low $\mathrm{SFR_{IR}}$s found in Section 4.1. Thus, our observation supports a nonevolving picture for the SFR–$L_\mathrm{[CII]}$ correlation in the star-forming clump-scale structure inside distant galaxies (Figure 5). This result suggests that the SFR–$L_\mathrm{[CII]}$ holds even for low-SFR and potentially metal-poor galaxies at high redshift.

4.2.2. Molecular Gas Mass

Previous studies showed that the [C II] 158 μm emission line is an excellent indicator of star-forming molecular gas. In particular, Zanella et al. (2018) showed a tight correlation between molecular gas masses (M_H2) and $L_\mathrm{[CII]}$ in $z \sim 2$ star-forming galaxies. Also, Dessauges-Zavadsky et al. (2020) examined whether the M_H2–$L_\mathrm{[CII]}$ relation is applicable to $4.5 < z < 5.5$ star-forming galaxies, and showed that the derived molecular gas masses are consistent with other methods. Using the method presented in Zanella et al. (2018), we estimated separately the molecular gas masses for the integrated, narrow [C II] and broad [C II] components (Table 1).

We also estimated the surface density of molecular gas mass Σ_H2. However, with the FWHM $\sim 0\rlap{.}''8$ resolution of the observation, both components of the [C II] emission are either unresolved or only marginally resolved. The most extreme case is found by assuming that the narrow [C II] is associated with the UV-bright component MACS0308-zD1.1, and assuming
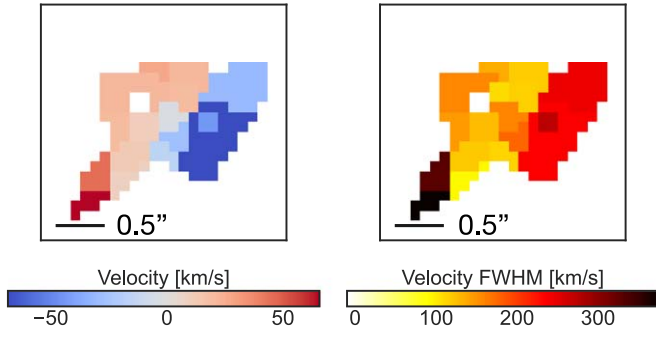
Figure 6. Left panel: velocity map of the [C II] emission line. The velocity zero-point is defined by the redshift of $z = 6.2078$. Right panel: velocity FWHM map of the [C II] emission line. Both maps are shown in the image plane. The velocity and FWHM maps are made by 1D Gaussian fitting to the spectra extracted from the moment-0 map image using pixels above $>2\sigma$ signals. The measured velocity difference and FWHM matches well with the spatially integrated measurement (Table 1). Both the velocity and the FWHM maps show a gradient toward the same direction, suggesting that the simple rotation kinematics does not explain multiple components of the [C II].

the size of the star-forming region is $r = 27$ pc (Welch et al. 2023). In this case, we found a remarkably dense surface gas mass density of $\log\,[\Sigma_{\rm H2}/(M_\odot\,{\rm pc}^2)] = 5.34 \pm 0.26$, which is >6000 times larger than that of giant molecular clouds in today's ISM (e.g., Leroy et al. 2008), and $\times 100$ higher than the maximum value found in the recent simulation of galaxies at $z \sim 8$ (Garcia et al. 2023).

Combined with the extremely high surface SFR density of $\Sigma_{\rm SFR} \sim 900\,M_\odot\,{\rm yr}^{-1}\,{\rm kpc}^{-2}$ (Welch et al. 2023), MACS0308-zD1.1 is located on the extreme edge of the Kennicutt–Schmidt relation (e.g., Kennicutt & Evans 2012). This might suggest that the UV-bright clump has a star formation environment similar to or more extreme than starburst galaxies.

4.3. [C II] Outflow or Another Structure?

We found multiple velocity components in the [C II] emission line: a narrow FWHM $\sim 110\,{\rm km\,s}^{-1}$ [C II] that is spatially coincident with the UV-bright star-forming region, and a broader FWHM $\sim 230\,{\rm km\,s}^{-1}$ [C II] that is spatially extended and potentially offset (Table 1). The offset both in centroid velocity and dispersion in the same region is difficult to explain with simple rotation (Figure 6).

As the narrow emission is spatially coincident with the UV emission of the galaxy, we associate it with the star formation activity of the UV-bright clump, MACS0308-zD1.1. Assuming a gas mass of $M_{\rm H2}/M_\odot = 5.1 \times 10^8$, and a radius of $r = 27$ pc, the line-of-sight velocity dispersion of a gas cloud will be $\sqrt{GM/3r} = 167\,{\rm km\,s}^{-1}$, assuming virial equilibrium, where G is the gravitational constant. This value is consistent with the measured line width of the narrow component, suggesting that the ISM is supported by internal turbulent motion of the gas cloud.

On the other hand, the origin of the broad [C II] emission is less clear. The broad line width and the velocity offset suggest that the broad [C II] emission line could arise from a physically distinct region from the narrow [C II] line. Additionally, the spatial extent of the broad [C II] component shows that the broad [C II] is spatially offset from the UV-bright star-forming region and the [C II] emission associated with the UV-bright clump. Although the estimated virial velocity of the cloud is uncertain without a confident size measurement, the fact that

the linewidth of the broad component appears super-virial suggests that this component of the gas cloud might not be bound. Combined with the extremely high density of star formation activity ($\Sigma_{\rm SFR} \sim 900\,M_\odot\,{\rm yr}^{-1}\,{\rm kpc}^{-2}$), circumstantial evidence suggests that the broad [C II] might arise from gas outflowing from the intense star-forming region, which is shown to exist in a larger >10 kpc scale (Fujimoto et al. 2020; Ginolfi et al. 2020; Pizzati et al. 2020, 2023).

An alternative interpretation of the broad [C II] component would be gas clumps generated as a result of the fragmentation of cold gas streams (i.e., inflow). Previous studies predicted such fragmentation of the cold gas streams in the inner halo ($\sim 0.2\,R_{\rm v}$), where $R_{\rm v}$ is the virial radius (e.g., Pallottini et al. 2017; Mandelker et al. 2018). After the fragmentation of cold gas streams, the masses of each clump are predicted to be order of $\sim 10^5$–$10^7\,M_\odot$. The estimated gas mass from our observation ($M_{\rm H2} \sim 5 \times 10^8\,M_\odot$) suggests that several clumps exist along the line of sight or the case that we are observing *down the barrel* of the stream, which increase observed gas mass and velocity width of the line.

More quantitative examination requires several follow-up observations, such as higher-resolution and higher-sensitivity ALMA [C II] follow-up and JWST's rest-frame optical emission to reveal the stellar distribution down to much deeper limits. Also, to examine the extremely dense environment of the star-forming ISM, ALMA observations using higher resolution or observations of a neutral dense gas indicator such as [O I] will be needed.

5. Conclusion

In this paper, we presented results of [C II] 158 μm emission line scan observations of a strongly lensed ($\mu \sim 20$) star-forming galaxy at $z \sim 6.2$. We detected the [C II] emission line within the expected frequency range. Additionally, no dust continuum was detected. Based on the observations, we found the following:

1. A spectroscopic redshift of $z = 6.2078 \pm 0.0002$ was determined, and the result is consistent with previous photometric redshift estimates (Salmon et al. 2020; Weaver et al. 2023).

2. The nondetection of the dust continuum emission suggests that MACS0308-zD1 is an almost dust-free environment. In particular, the UV-bright clump, MACS0308-zD1.1, has little dust-obscured SFR of $<0.1\,M_\odot\,{\rm yr}^{-1}$, and a low dust-obscured fraction of $<3\%$. The low dust-obscured activity is in stark contrast compared with the observations of other relatively massive $M_* > 10^{9.5}\,M_\odot$ star-forming galaxies (Fudamoto et al. 2020; Schouws et al. 2022), and suggests that the stellar populations in this galaxy are young and metal-poor.

3. From the relatively bright detection of the [C II] emission line, we found that MACS0308-zD1 is consistent with the nonevolving SFR–$L_{\rm [CII]}$ correlation (De Looze et al. 2014; Schaerer et al. 2020). Also, the bright [C II] emission suggests that the star-forming region of the galaxy may have an extremely dense molecular gas environment of $\log\,[\Sigma_{\rm H2}/(M_\odot\,{\rm pc}^2)] = 5.34 \pm 0.26$. With the extremely high density of star formation activity of $\Sigma_{\rm SFR} \sim 900\,M_\odot\,{\rm yr}^{-1}\,{\rm kpc}^{-2}$, the UV-bright star-forming region of MACS0308-zD1.1 is located in

the most extreme edge of the Kennicutt–Schmidt relation (Kennicutt & Evans 2012).

4. We found that the [C II] emission line can be decomposed into two components; the narrow line (FWHM $= 110 \pm 20\,\mathrm{km\,s^{-1}}$) and the broad line (FWHM $= 230 \pm 50\,\mathrm{km\,s^{-1}}$).

The broad component is blueshifted with respect to the narrow component with a velocity offset of $\Delta v = -80 \pm 20\,\mathrm{km\,s^{-1}}$. Although higher spatial resolution (e.g., matched to the Hubble Space Telescope, hereafter HST, and JWST resolutions of $\sim 0\rlap.{''}16$) and higher sensitivity observations are required to conclude, the narrow component is most likely associated with a gravitationally bound gas cloud with intense star-forming activity, as seen by the UV-bright clump, and the broad component may belong to kinematically and spatially distinct activity in the galaxy (e.g., possibly outflowing gas).

This spectroscopic redshift confirmation of a strongly lensed L_* star-forming galaxy MACS0308-zD1 at $z = 6.2078$ demonstrates viability of the future follow-up ALMA observations. Furthermore, JWST's NIRSpec IFU observation will be critical to understand the morphologically and kinematically complex structure of this galaxy. With the large magnification of $\mu \sim 20$, MACS0308-zD1 will serve as a unique test case to study low-SFR and low-mass galaxy growths in great detail in the future observations.

ORCID iDs

Yoshinobu Fudamoto ⓘ https://orcid.org/0000-0001-7440-8832
Akio K. Inoue ⓘ https://orcid.org/0000-0002-7779-8677
Dan Coe ⓘ https://orcid.org/0000-0001-7410-7669
Brian Welch ⓘ https://orcid.org/0000-0003-1815-0114
Ana Acebron ⓘ https://orcid.org/0000-0003-3108-9039
Massimo Ricotti ⓘ https://orcid.org/0000-0003-4223-7324
Nir Mandelker ⓘ https://orcid.org/0000-0001-8057-5880
Rogier A. Windhorst ⓘ https://orcid.org/0000-0001-8156-6281
Xinfeng Xu ⓘ https://orcid.org/0000-0002-9217-7051
Yuma Sugahara ⓘ https://orcid.org/0000-0001-6958-7856
Franz E. Bauer ⓘ https://orcid.org/0000-0002-8686-8737
Maruša Bradač ⓘ https://orcid.org/0000-0001-5984-0395
Larry D. Bradley ⓘ https://orcid.org/0000-0002-7908-9284
Jose M. Diego ⓘ https://orcid.org/0000-0001-9065-3926
Michael Florian ⓘ https://orcid.org/0000-0001-5097-6755
Brenda Frye ⓘ https://orcid.org/0000-0003-1625-8009
Seiji Fujimoto ⓘ https://orcid.org/0000-0001-7201-5066
Takuya Hashimoto ⓘ https://orcid.org/0000-0002-0898-4038
Alaina Henry ⓘ https://orcid.org/0000-0002-6586-4446
Guillaume Mahler ⓘ https://orcid.org/0000-0003-3266-2001
Pascal A. Oesch ⓘ https://orcid.org/0000-0001-5851-6649
Swara Ravindranath ⓘ https://orcid.org/0000-0002-5269-6527
Jane Rigby ⓘ https://orcid.org/0000-0002-7627-6551
Keren Sharon ⓘ https://orcid.org/0000-0002-7559-0864
Victoria Strait ⓘ https://orcid.org/0000-0002-6338-7295
Yoichi Tamura ⓘ https://orcid.org/0000-0003-4807-8117
Michele Trenti ⓘ https://orcid.org/0000-0001-9391-305X
Eros Vanzella ⓘ https://orcid.org/0000-0002-5057-135X
Erik Zackrisson ⓘ https://orcid.org/0000-0003-1096-2636
Adi Zitrin ⓘ https://orcid.org/0000-0002-0350-4488

References

Acebron, A., Cibirka, N., Zitrin, A., et al. 2018, ApJ, 858, 42
Akins, H. B., Fujimoto, S., Finlator, K., et al. 2022, ApJ, 934, 64
Algera, H. S. B., Inami, H., Oesch, P. A., et al. 2023, MNRAS, 518, 6142
Astropy Collaboration, Price-Whelan, A. M., Lim, P. L., et al. 2022, ApJ, 935, 167
Bakx, T. J. L. C., Sommovigo, L., Carniani, S., et al. 2021, MNRAS, 508, L58
Bakx, T. J. L. C., Tamura, Y., Hashimoto, T., et al. 2020, MNRAS, 493, 4294
Béthermin, M., Fudamoto, Y., Ginolfi, M., et al. 2020, A&A, 643, A2
Bouwens, R., González-López, J., Aravena, M., et al. 2020, ApJ, 902, 112
Bouwens, R. J., Smit, R., Schouws, S., et al. 2022, ApJ, 931, 160
Bradač, M., Garcia-Appadoo, D., Huang, K.-H., et al. 2017, ApJL, 836, L2
Calura, F., Vanzella, E., Carniani, S., et al. 2021, MNRAS, 500, 3083
Carniani, S., Ferrara, A., Maiolino, R., et al. 2020, MNRAS, 499, 5136
CASA Team, Bean, B., Bhatnagar, S., et al. 2022, PASP, 134, 114501
Chabrier, G. 2003, PASP, 115, 763
Coe, D., Salmon, B., Bradač, M., et al. 2019, ApJ, 884, 85
De Looze, I., Cormier, D., Lebouteiller, V., et al. 2014, A&A, 568, A62
Dessauges-Zavadsky, M., Ginolfi, M., Pozzi, F., et al. 2020, A&A, 643, A5
Faisst, A. L., Schaerer, D., Lemaux, B. C., et al. 2020, ApJS, 247, 61
Fudamoto, Y., Inoue, A. K., & Sugahara, Y. 2023, MNRAS, 521, 2962
Fudamoto, Y., Oesch, P. A., Faisst, A., et al. 2020, A&A, 643, A4
Fudamoto, Y., Oesch, P. A., Schouws, S., et al. 2021, Natur, 597, 489
Fudamoto, Y., Smit, R., Bowler, R. A. A., et al. 2022, ApJ, 934, 144
Fujimoto, S., Oguri, M., Brammer, G., et al. 2021, ApJ, 911, 99
Fujimoto, S., Silverman, J. D., Bethermin, M., et al. 2020, ApJ, 900, 1
Gaia Collaboration, Vallenari, A., Brown, A. G. A., et al. 2023, A&A, 674, A1
Garcia, F. A. B., Ricotti, M., Sugimura, K., & Park, J. 2023, MNRAS, 522, 2495
Ginolfi, M., Jones, G. C., Béthermin, M., et al. 2020, A&A, 633, A90
Glazer, K., Bradac, M., Sanders, R. L., et al. 2023, arXiv:2309.11548
Harikane, Y., Ouchi, M., Inoue, A. K., et al. 2020, ApJ, 896, 93
Hashimoto, T., Inoue, A. K., Mawatari, K., et al. 2019, PASJ, 71, 71
Hashimoto, T., Laporte, N., Mawatari, K., et al. 2018, Natur, 557, 392
Heintz, K. E., Watson, D., Oesch, P. A., Narayanan, D., & Madden, S. C. 2021, ApJ, 922, 147
Inami, H., Algera, H. S. B., Schouws, S., et al. 2022, MNRAS, 515, 3126

Inoue, A. K., Shimizu, I., Tamura, Y., et al. 2014, ApJL, 780, L18
Jones, G. C., Vergani, D., Romano, M., et al. 2021, MNRAS, 507, 3540
Kennicutt, R. C., & Evans, N. J. 2012, ARA&A, 50, 531
Killi, M., Watson, D., Fujimoto, S., et al. 2023, MNRAS, 521, 2526
Knudsen, K. K., Richard, J., Kneib, J.-P., et al. 2016, MNRAS, 462, L6
Le Fèvre, O., Béthermin, M., Faisst, A., et al. 2020, A&A, 643, A1
Leroy, A. K., Walter, F., Brinks, E., et al. 2008, AJ, 136, 2782
Liang, L., Feldmann, R., Murray, N., et al. 2023, MNRAS, in press
Madau, P., & Dickinson, M. 2014, ARA&A, 52, 415
Maiolino, R., Gallerani, S., Neri, R., et al. 2012, MNRAS, 425, L66
Mandelker, N., van Dokkum, P. G., Brodie, J. P., van den Bosch, F. C., &
    Ceverino, D. 2018, ApJ, 861, 148
Matthee, J., Sobral, D., Boogaard, L. A., et al. 2019, ApJ, 881, 124
Molyneux, S. J., Smit, R., Schaerer, D., et al. 2022, MNRAS, 512, 535
Pallottini, A., Ferrara, A., Gallerani, S., et al. 2017, MNRAS, 465, 2540
Pizzati, E., Ferrara, A., Pallottini, A., et al. 2020, MNRAS, 495, 160
Pizzati, E., Ferrara, A., Pallottini, A., et al. 2023, MNRAS, 519, 4608
Salmon, B., Coe, D., Bradley, L., et al. 2020, ApJ, 889, 189

Schaerer, D., Boone, F., Zamojski, M., et al. 2015, A&A, 574, A19
Schaerer, D., Ginolfi, M., Béthermin, M., et al. 2020, A&A, 643, A3
Schouws, S., Stefanon, M., Bouwens, R., et al. 2022, ApJ, 928, 31
Sommovigo, L., Ferrara, A., Pallottini, A., et al. 2022, MNRAS, 513, 3122
Stefanon, M., Labbé, I., Oesch, P. A., et al. 2021, ApJS, 257, 68
Sugahara, Y., Inoue, A. K., Fudamoto, Y., et al. 2022, ApJ, 935, 119
Tamura, Y., Mawatari, K., Hashimoto, T., et al. 2019, ApJ, 874, 27
Treu, T., Roberts-Borsani, G., Bradac, M., et al. 2022, ApJ, 935, 110
Vallini, L., Gallerani, S., Ferrara, A., Pallottini, A., & Yue, B. 2015, ApJ,
    813, 36
Vanzella, E., Calura, F., Meneghetti, M., et al. 2019, MNRAS, 483, 3618
Vanzella, E., Claeyssens, A., Welch, B., et al. 2023, ApJ, 945, 53
Watson, D., Christensen, L., Knudsen, K. K., et al. 2015, Natur, 519, 327
Weaver, J. R., Davidzon, I., Toft, S., et al. 2023, A&A, 677, A184
Welch, B., Coe, D., Zitrin, A., et al. 2023, ApJ, 943, 2
Witstok, J., Smit, R., Maiolino, R., et al. 2022, MNRAS, 515, 1751
Zanella, A., Daddi, E., Magdis, G., et al. 2018, MNRAS, 481, 1976
Zitrin, A., Fabris, A., Merten, J., et al. 2015, ApJ, 801, 44